Accepted Manuscript

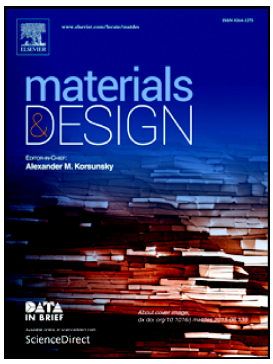

Endurance testing of the additively manufactured STAR resistojet

M. Robinson, A. Grubišić, G. Rempelos, F. Romei, C. Ogunlesi, S. Ahmed

PII: S0264-1275(19)30345-4
DOI: https://doi.org/10.1016/j.matdes.2019.107907
Article Number: 107907
Reference: JMADE 107907

To appear in: *Materials & Design*

Received date: 13 February 2019
Revised date: 22 May 2019
Accepted date: 30 May 2019

Please cite this article as: M. Robinson, A. Grubišić, G. Rempelos, et al., Endurance testing of the additively manufactured STAR resistojet, Materials & Design, https://doi.org/10.1016/j.matdes.2019.107907

Endurance Testing of the Additively Manufactured STAR Resistojet

M. Robinson[1], A. Grubišić[2], G. Rempelos[2], F. Romei[2], C. Ogunlesi[2], S. Ahmed[3]
[1]Corresponding author. Email address: m.d.robinson@soton.ac.uk. University of Southampton, Southampton, SO17 1BJ, UK
[2]University of Southampton, Southampton, SO17 1BJ, UK
[3]Diamond Light Source, Rutherford Appleton Laboratories, UK

Abstract

This paper reports the outcome of endurance tests performed on a proof-of-concept design of a high-temperature resistojet thruster. A high-performance resistojet could enable a fully all-electric spacecraft architecture providing all propulsion system functions. The thruster utilises a novel additive-manufactured heat exchanger, consisting of concentric thin-walled cylinders, which act as both a resistive heating element and regenerative heat exchanger. Two complete thruster assemblies were tested, with heat exchangers manufactured from 316L stainless steel using selective laser melting. The two test units were used to investigate the operational endurance and determine life-limiting failure modes of the design. The tests consisted of repeated operational cycling to known temperature limits while under vacuum. Degradation and failure was inferred from electrical characteristics of the thrusters, and X-ray computed tomography imaging was used for non-destructive inspection both pre- and post-testing. The analysis showed that the failure modes are due to thermally-induced stresses resulting from mechanical constraints and temperature gradients. The failures occurred after approximately 40 cycles in the first thruster operating with a current of 25 A, and, in the second thruster, after a total of 300 cycles at 15 A and 217 cycles at 20 A, resulting in two distinctly different failure locations.

Keywords: resistojet; spacecraft propulsion; additive manufacturing; x-ray CT; all-electric spacecraft; endurance testing

Acronyms/Abbreviations

AM	Additive manufacturing, additive-manufactured
CVD	Chemical vapour deposition
DCGA	DC Gain Accuracy
GEO	Geocentric/Geosynchronous Earth Orbit
LEO	Low Earth Orbit
OA	Offset Accuracy
RCS	Reaction Control System
SLM	Selective laser melting
SSTL	Surrey Satellite Technology Limited
STAR	Super-high Temperature Additive-manufactured Resistojet
TPR	Thrust-to-power ratio

List of Symbols

I_{sp}	Specific impulse	s
Δv	Change in spacecraft velocity	ms^{-1}
T_n	Temperature in resistojet divergent nozzle section (see Figure 2)	°C
P_e	Electrical power dissipated in resistojet	W
R	Resistance across resistojet	mΩ

1. Introduction

Hall effect (HET) and gridded ion (GIT) thrusters are relatively mature electric spacecraft propulsion technologies, offering high specific impulse (I_{sp}) while operating on inert xenon propellant. These systems have enabled high-energy interplanetary missions such as the BepiColombo mission to Mercury [1]. Electric propulsion has become widely utilised in the role of primary propulsion for station keeping of commercial GEO (Geocentric/Geosynchronous Earth Orbit) telecommunications satellites. More recently, spacecraft have also utilised electric propulsion for orbit raising to GEO in addition to station keeping, in a bid

to increase useful payload mass, and are termed “all-electric” systems. Several “all-electric” spacecraft have been launched in recent years, such as Eutelsat 115 West B and ABS-3A based on the Boeing 702SP bus, and SES-12 and Eutelsat 172B based on the Airbus E3000 EOR bus. Many more are planned and in construction, with new platforms being developed such as OHB’s Electra SmallGEO bus. These spacecraft are however often required to carry a secondary chemical or cold gas propulsion system to deliver reaction control system (RCS) functions, which increases system complexity and can introduce additional costs due to the hazardous nature of chemical propellants. There is a need in the space propulsion field to develop a suitable high thrust-to-power ratio (TPR) electric propulsion system to remove the requirement for conventional hazardous chemical propulsion systems, whilst operating from a common inert propellant with the primary. Such an architecture has been proposed by Coletti et al. [2], and has many benefits over purely chemical or combined chemical and electric architectures, as described by Grubišić et al [3].

The resistojet, a class of electrothermal thruster, has been identified as an attractive candidate technology for electric RCS thrusters. They offer the potential for high TPR, with low absolute power, and reduced electrical complexity compared to other electric propulsion technologies that require high voltages or high-frequency AC supplies. Serving as a practical auxiliary propulsion system in combination with electric primary propulsion, a high-performance resistojet could enable a fully all-electric spacecraft architecture providing all propulsion system functions. Resistojets have a long history of use in multiple roles, including station-keeping (on Intelsat V) and orbit adjustment (on the Iridium constellation) [4]. They are used today by SSTL (Surrey Satellite Technology Ltd.) as a primary propulsion system for small LEO (Low Earth Orbit) satellites, where they serve as the sole propulsion system and are used primarily for orbit reboost and constellation phasing. Their utility, both in this role and as a component of an all-electric architecture, is currently limited by their low specific impulse when operating with propellants commonly used by HET and GIT systems such as xenon. In spite of this, xenon is still a common propellant for LEO resistojets due to its high storage density (hence, high impulse density). The high molecular mass results in a high TPR but low I_{sp} – a desirable trait in high-I_{sp} electrostatic propulsion systems, but detrimental to electrothermal thrusters which give low I_{sp} with heavy xenon propellant. However, small spacecraft are often volume constrained rather than mass constrained, therefore the high impulse density of xenon can be attractive despite its lower I_{sp}. Commercially available resistojets such as the SSTL T-50 achieve 48 s I_{sp} with xenon, operating at maximum heater temperatures of approximately 600 °C [5]. Significant propellant mass savings could be made by increasing the operating temperature of resistojets beyond the current state of the art while still benefiting from a high impulse density.

1.1 The STAR Thruster Development Program

Resistojets generate heat by passing an electric current through a resistive element, thereby heating a propellant at high pressure, which is subsequently expanded through a nozzle resulting in a supersonic exhaust jet. A simplified relation for specific impulse of a thermal rocket (regardless of the energy source) is shown in Equation 1, where η_n is a total nozzle efficiency relative to ideal isentropic expansion, C_p is the propellant constant pressure specific heat capacity, and T_0 is the stagnation temperature of the propellant at the nozzle inlet [6]. The relation shows that, for a given nozzle design and propellant properties, an increase in I_{sp} can be achieved only by increasing the stagnation temperature of the propellant. This implies that the performance of a resistojet is limited by the thermal design of the heater and the material from which it is made.

$$I_{sp} \approx \frac{\eta_n}{g_0}\sqrt{2C_pT_0} \qquad 1$$

The Super-high Temperature Additive-manufactured Resistojet (STAR) project at the University Of Southampton has a requirement to reach 80 s I_{sp} using xenon propellant, with a reaching goal of 95 s. This increase of at least 66 % in I_{sp} represents a step change in resistojet performance compared to current commercial offerings, corresponding directly to reduced propellant load/cost or extended mission life. In combination with their simplicity and compactness, this increased performance makes resistojets an attractive candidate technology for all-electric spacecraft or robust primary propulsion systems for small satellites. In order to achieve the required performance, the final STAR thruster must reach a minimum T_0 of roughly 2100 °C, up to 3000 °C for the higher performance goal, with somewhat greater maximum structural temperatures depending on the effectiveness of heat transfer from the heater to the propellant. This represents a great materials and design challenge, demanding the use of refractory materials to withstand these temperatures, as well as effective design to reduce the maximum material temperature and prevent excessive thermal losses. The prototype thruster design is detailed in Section 2.

The prototype design is the result of several years of development at the University of Southampton, as documented by Romei et al. [7]. During this process, the concentric cylinder resistojet design has been developed from a concept to a prototype utilising an iterative design process in which a COMSOL multiphysics model combines the electric, thermal and fluid dynamics of the resistojet [8] [9]. Four prototype thruster assemblies with a novel additive-manufactured (AM) heat exchanger have been manufactured in 316L stainless steel at the University of Southampton using a Concept Laser M2 selective laser melting (SLM) machine, demonstrating that SLM is a viable manufacturing method for the intricate microchannels of the resistojet [6]. X-ray computed tomography (CT) has successfully been used to non-destructively inspect and evaluate the additive-manufactured (AM) parts. Romei et al have experimentally demonstrated that the 316L prototype thrusters can achieve performance equivalent

to the commercially available state of the art [10]. The first prototype parts have been produced in tantalum, demonstrating the manufacture of the refractory metals that will be required for high performance. Analysis of these parts has been undertaken by Ogunlesi [11]. In parallel, the 316L prototypes are being tested to investigate the suitability of the design for environmental qualification. This paper reports on endurance testing of the thruster, to investigate life-limiting failure modes.

The University of Southampton is working closely with Surrey Satellite Technology Ltd. (SSTL) in order to ensure the STAR thruster system meets commercially relevant performance and environmental requirements. Two of the prototype thrusters manufactured from 316L have been subjected to endurance tests – these assemblies will be referred to as STAR-0-B and STAR-0-C. Although the material is not that which will be used in a flight system, early tests were undertaken to expose any failure modes inherent to the design, as well as to provide validation data for the multiphysics models. This information will be used in the next generation design to eliminate or mitigate these failure modes. SSTL has provided a set of requirements related to the potential mission scenarios envisaged for the resistojet – primary propulsion on a small LEO platform, and auxiliary propulsion on a large all-electric GEO platform. For the small LEO platform application, SSTL indicates a thrust requirement in the range of 20-50 mN thrust and a minimum 23.5 kNs total impulse (corresponding to 30 kg xenon propellant load utilised at 80 s I_{sp}). Therefore, depending on thrust, the thruster must withstand a total of 130-326 hours of hot firing. If used at 20 mN, SSTL indicates that each manoeuvre will have a hot firing duration of at least 5 minutes, resulting in a requirement of ~4000 thermal cycles (heating from ambient temperature to operating temperature, and subsequent cooling).

1.2 Previous literature

A review of the literature surrounding resistojet endurance testing was conducted in order to survey test methods and investigate relevant failure modes. Sparse literature exists related to the endurance testing of resistojets, and even less so for concentric cylindrical designs in particular. However, a small number of papers provide results of interest to endurance testing the STAR thruster.

Pfeifer [12] reports a life test of a family of resistojets developed by the Marquardt Company in the 1960s and 1970s. These resistojets used a concentric regenerative design similar to STAR, however with a very different manufacturing method. Pure rhenium cylinders were manufactured by chemical vapour deposition (CVD) and joined via connecting struts using electron beam welding. Two thrusters of identical design were tested using ammonia and hydrogen propellant respectively. The tests had a total firing duration of 360 hours, with cycles of 30 minutes firing at 220 W and 30 minutes cooling. This is equivalent to the upper lifetime limit required by SSTL for a small LEO satellite (see Section 1.1). However, due to the longer firing time in Pfeiffer's paper, the cycle requirement is less than one fifth of the STAR requirement. This could conceivably be either beneficial or adverse for the thruster life, depending on whether failure is dominated by number of cycles to fatigue failure, or by material effects of long-duration exposure to high temperature.

Pfeifer monitored gas pressure and mass flow, electrical power and resistance during testing, to detect any deviation from nominal operation. The ammonia resistojet suffered no failures over its full lifetime at full power. The hydrogen resistojet on the other hand exhibited short-circuiting after 76 hours. It was discovered that the bellows, built into the assembly to allow free thermal expansion of the concentric cylinders, had been unable to function due to a binding between one of the cylinders and a support component. This caused the inner cylinder to buckle due to build-up of thermal compressive stresses, contacting the next cylinder and causing a short circuit. Marquardt continued the test in a low-power mode to simulate remedial action if such a failure were discovered on-orbit, rendering replacement impossible. This failure mode is directly relevant to STAR, since the current design incorporates no means of limiting thermomechanical stress during operation.

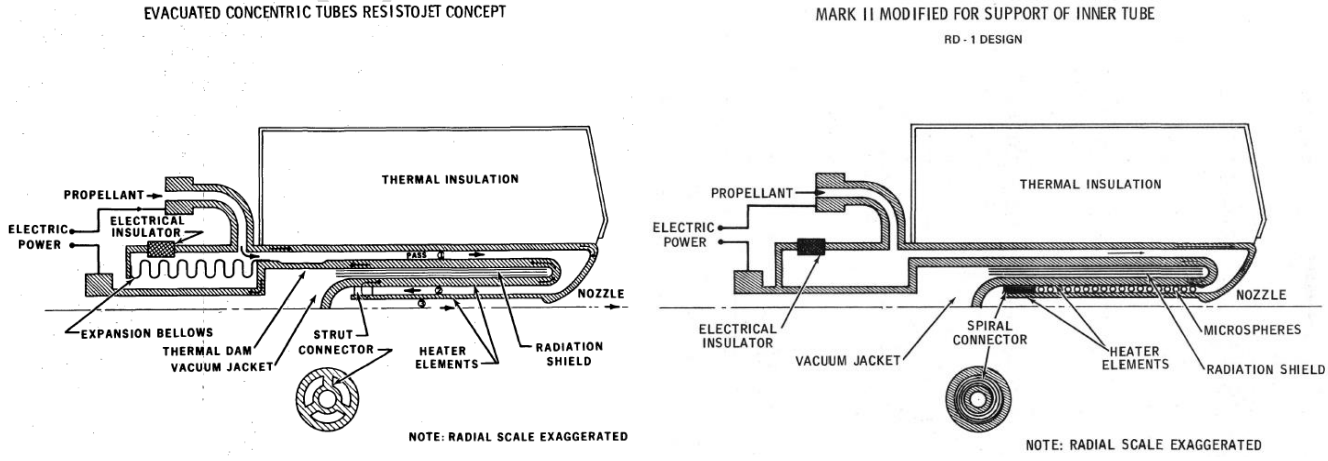

Figure 1: Biowaste resistojet designs showing replacement of bellows with inner cylinder support. Reproduced from Fig. 1 (left) and Fig. 66 (right) of Philips [13].

Following the tests reported by Pfeifer, a technical report by Philips [13], also of the Marquardt Company, describes design changes implemented to alleviate the buckling problem and remove the bellows (see Figure 1). To replace the bellows, the rigid strut connectors between the inner and second cylinders are replaced by a thin conducting spiral strip, allowing differential expansion of the two cylinders. In addition, to physically prevent buckling, the space between the two cylinders is packed with ceramic microspheres. Philips writes that the new design was later tested for endurance.

Page et al. [14] describe an ongoing endurance test on six cylindrical resistojets. These are of a similar design to those reported by Pfeifer and Philips, though with different manufacturing techniques. The resistojets of Page used rolled and welded sheet tubes, rather than CVD. Page's report details a number of expected failure modes, such as sublimation and redeposition of heater material causing blockages in cooler areas, stress rupture, creep, and cyclic fatigue. At the time of writing, none of these failures had been seen in any of their thrusters after 5000 hours of operation in the thrusters using ammonia, and 3000 hours operation on the hydrogen thrusters, using the same test protocol as Pfeifer. This is an indication that, in principle, a concentric cylinder resistojet can last for an order of magnitude greater firing time, and up to the number of thermal cycles required by STAR. It should be noted that STAR does not currently incorporate thermal stress prevention features such as bellows. Page et al do report that two of their three hydrogen thrusters developed leaks between 1500 and 2000 hours, due to 'frequent touching' of the outer elements during the start-up thermal transient. They do not describe this problem further. Following Page's report, Yoshida et al. [15] summarise the final results at the end of the endurance test in a brief article. The ammonia thrusters reportedly suffered no failures during the full 8000-hour test. They reiterate the two leaking hydrogen thrusters described by Page, but also do not elaborate further, except for attributing the failures to "experimental fabrication techniques… not associated with the hydrogen propellant". They substituted another hydrogen thruster for one of the leaking ones, which accrued 6000 hours of nominal firing thereafter.

Morren et al. [16] report on a resistojet design utilising a platinum tube coil radiative heater, which at their time of writing had sustained 1400 operating cycles over 1160 hours of firing (~ 50 minutes heating per cycle). During early tests, their coil was unable to support its own weight due to high-temperature softening. This should not occur in the STAR, since the cylinders are shorter than the platinum coil, and better supported. Furthermore, the STAR is tested in a vertical position, as opposed to the horizontal position reported by Morren. Slutz [17] reports a 10000 hour life test on an evolved version of Morren's design. This test used much longer cycles than the others so far reported, at 72 hours of heating, resulting in only 141 cycles. The design and conditions are not necessarily enlightening for STAR, however, Slutz describes an interesting method to simulate zero-gravity average conditions, by mounting the thruster vertically and periodically inverting the direction of mounting.

2. STAR Thruster Design

The present prototype thruster design was developed by Romei and Grubišić [6]. Figure 2 shows a sectioned image of the prototype assembly, including a detail view showing the monolithic AM regenerative heat exchanger component. The thruster consists of the heat exchanger, electron beam welded at the nozzle to a conventionally machined outer pressure case, and at its other end to an AM propellant inflow component. These components are all manufactured from 316L stainless steel in this prototype. The AM parts were manufactured on a Concept Laser M2 machine, using CL 20ES 316L powder with particle size in the range of 10-45 µm. The parts were manufactured using a laser power of 177 W, with laser speed of 800 mms^{-1} for bulk area and 1600 mms^{-1} for borders, using a meander exposure strategy. A spacer (item 3 in Figure 2), manufactured from Macor machinable ceramic, forms an electrically insulating mechanical support for the heat exchanger, preventing gas flow from bypassing the heat exchanger. A ceramic collar (item 4 in Figure 2) electrically isolates the bolted flange, in combination with ceramic sleeves and washers on each bolt. This isolation is required to create the electrical circuit through the heat exchanger, with the machined case forming one terminal and the inflow the other. Three M3 screws are used to mount the thruster to its test stand with the use of ceramic sleeves and washers for electrical and thermal isolation.

For the purpose of this paper, the most important component is the monolithic AM heat exchanger with integrated nozzle. This component consists of several concentric cylinders connected by supports allowing the passage of propellant between annular microchannels. The component has multiple functions: generating high temperatures by electrical dissipation, heat transfer to the fluid, regenerative heat capture from the assembly and accelerating the flow to high velocity in a supersonic nozzle. The concentric walls have varying cross-sectional area, decreasing towards the centre of the component, giving rise to a higher

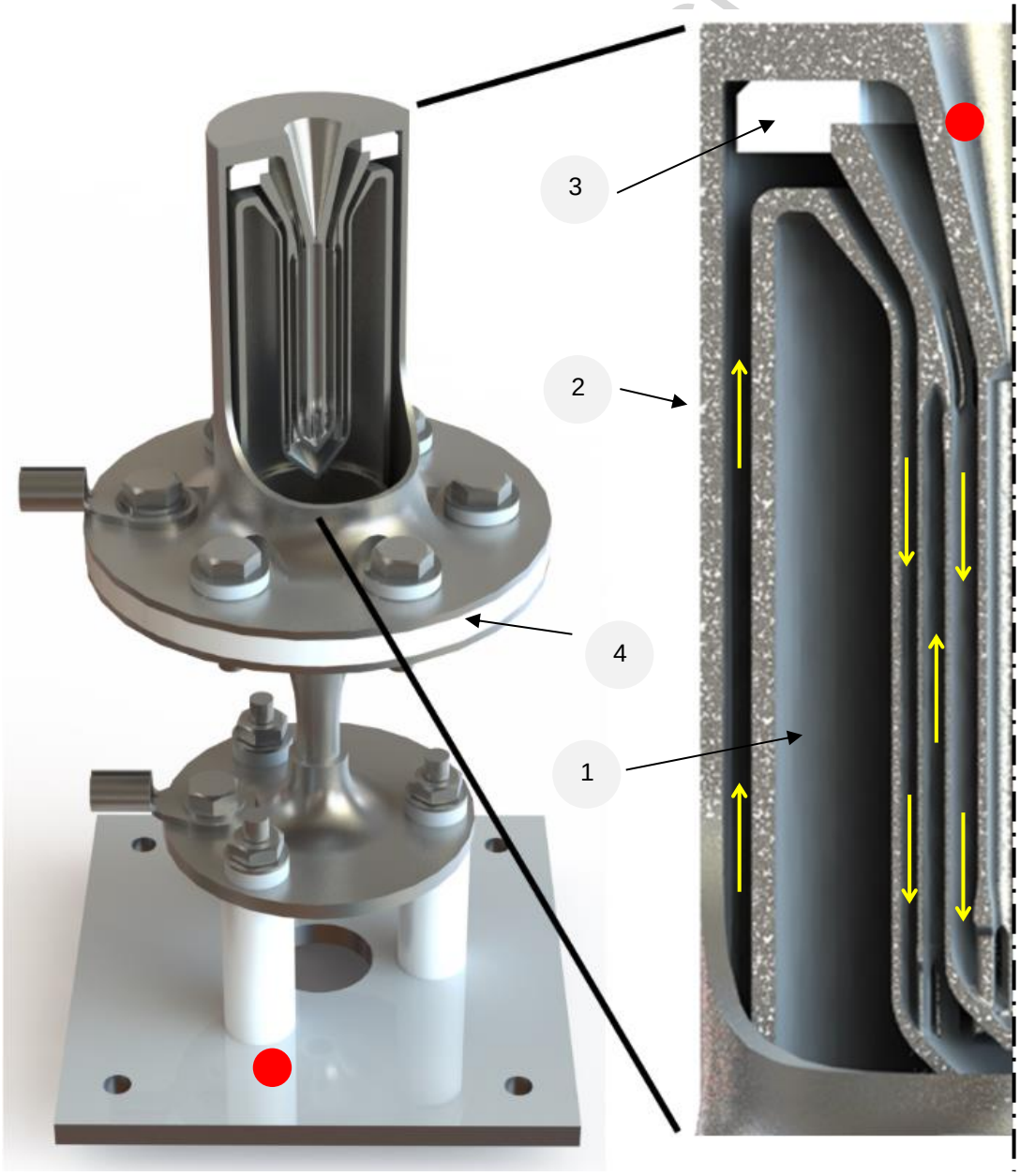

Figure 2: Rendered CAD cutaway of STAR thruster prototype. Labelled features: 1 - AM heat exchanger/nozzle, 2 - pressure case, 3 – ceramic nozzle spacer, 4 – ceramic collar. Yellow arrows indicate propellant gas flow and red dots indicate positions of thermocouples. Metal plate at bottom left is 58 x 58 mm and assembly height is 107 mm.

heating power density for a given operating current whilst reducing conductive heat loss to the exterior of the resistojet. The propellant circulates through the cylinders as shown in Figure 2, increasing residence time for the gas to maximise heating, and using the cold inlet propellant to regeneratively cool the outer case. These design features combine to give a high thermal efficiency.

Table 1 shows the cross-sectional areas of each of the five concentric cylinders in the heat exchanger, shown graphically in Figure 3. Since resistance is inversely proportional to cross-sectional area of the conductor, a simple comparison of the contribution of each cylinder to the total cold resistance of the heat exchanger can be made, with the simplifying assumption that all cylinders are of the same length and neglecting the contribution of the connecting struts. The two innermost cylinders contribute over 65 % of the cold resistance, indicating that most of the power is deposited in this region, since for a constant current, dissipated power is directly proportional to resistance.

Table 1: Cross-sectional area of resistojet heat exchanger cylinders, resistance relative to innermost cylinder, and resistance relative to sum of cylinders.

Cylinder number	Cross-sectional area (mm^2)	R/R_{inner}	R/R_{total}
1 (inner)	1.82	1	0.359
2	2.06	0.883	0.317
3	2.96	0.614	0.220
4	7.47	0.243	0.087
5 (outer)	43.23	0.042	0.015

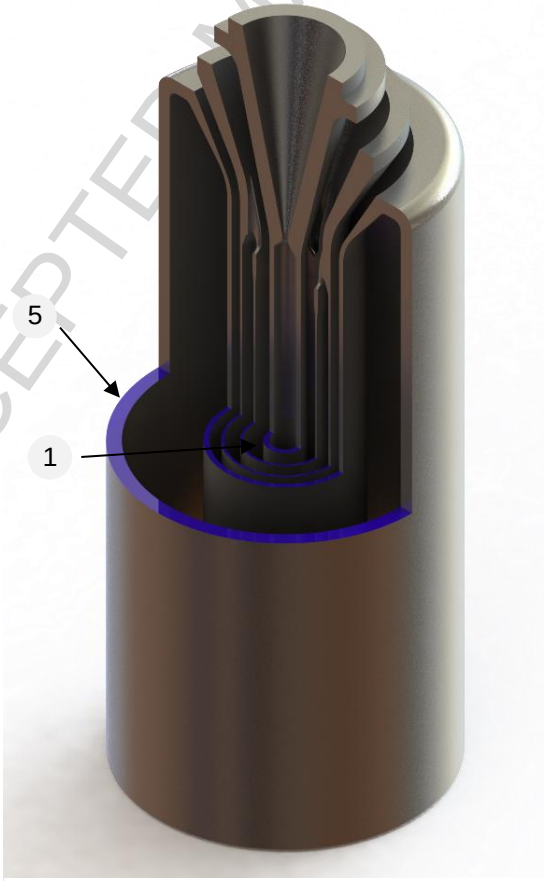

Figure 3: Cutaway of AM heat exchanger showing cross-sectional areas for electric current in blue. Outer wall diameter is 18 mm.

3. Test Methodology

Based on the literature around high-temperature resistojet failure modes (see Section 1.2) and analysis of the design, it was considered most likely that life-limiting failure modes would result from the effects of high temperature, and stresses induced by temperature gradients. In particular, large thermal stresses develop in the centre of the resistojet, due to a combination of high temperature gradients between concentric cylinders, and mechanical constraint of the innermost cylinder which limits thermal expansion. Combined with the effects of high temperature on material properties, which include both instantaneous strength reduction when at high temperature, and effects of prolonged temperature exposure such as annealing and carbide precipitation, it was anticipated that mechanical failure of the inner cylinder was the most probable failure mode.

It was estimated that mechanical stress from propellant gas pressure would contribute little to any failure modes observed in the thruster. This is justified in Table 2, which describes the hoop stress in each of the walls of the thruster as shown in Section 2, assuming that the pressure difference across that wall was equal to the maximum engine operating pressure (4 bar), which in practice would not occur. Even in this bounding case, the maximum hoop stress, 8.16 MPa, is less than 10 % of the yield strength of 316L at 650 °C [18]. Based on its measured performance, the maximum temperature in the 316L resistojet is not expected to exceed this [10]. It was concluded that the thruster was unlikely to fail due to internal pressure directly, thus propellant was not used in these initial tests. Furthermore, operating without propellant causes higher temperatures in the resistojet, making the endurance tests conservative with respect to the operational conditions.

Table 2: Hoop stress in resistojet tubes assuming 100 % pressure drop across wall (4 bar)

Wall inner radius (mm)	Wall thickness (mm)	Hoop stress (MPa)
0.81	0.3	1.08
2.11	0.15	5.63
3.06	0.15	8.16
3.81	0.3	5.08
8.2	0.8	4.1

Endurance tests were conducted as follows: the resistojet prototypes were placed under vacuum of at least 10^{-1} mbar, and subjected to repeating cycles of a heating period (power on) and a cooling period (power off), lasting 5 minutes and 15 minutes respectively. The heating time is based on operational requirements (see Section 1.1), while the cooling time was chosen to obtain a large temperature drop while maximising the number of cycles possible in the timeframe of the experiment. No propellant gas was supplied to the thruster during the tests. The thrusters were tested either until failure was observed, or otherwise for the maximum time available in the test chamber. Table 3 shows the different current levels applied for each test. STAR-0-B was tested at a high current of 25 A, corresponding to the expected operating point of the thruster. Following this, STAR-0-C was tested initially at lower currents, moving to higher currents. The power supply unit (PSU) was run in current controlled mode, with a prescribed voltage limit to prevent equipment damage in a failure scenario. Prior to and after testing, each thruster was inspected using micro x-ray computed tomography (CT) scanning, carried out at the University of Southampton in the μ-VIS X-Ray Imaging Centre, on a modified Nikon XTEK XT H 225 microfocus CT system. All scans were taken with 25 μm voxel linear dimension.

Table 3: Endurance test protocol. All tests follow a 5-minute heating, 15-minute cooling cycle.

Thruster	Heating current (A)	PSU voltage limit (V)	Number of planned cycles
STAR-0-B	25	6	500
STAR-0-C	15	3	300
	20	3	300
	25	6	300

During testing, current and voltage were measured at the resistojet terminals at a sample rate of 4 Hz, this frequency being chosen to allow the LabVIEW script to complete all operations in each loop. From this, the electrical resistance of the thruster was calculated and utilised as an indicative diagnostic measurement. Since the resistance of the thruster is fully determined by the (temperature-dependent) material resistivity and the geometry of the resistive structure, it was reasoned that any changes in the resistance not correlated with changes in temperature would be indicative of changes to the resistojet structure – i.e. potential failures. For example, contact between any of the concentric cylinders would result in a short circuit, showing a rapid drop in resistance, whereas fracture of the connecting struts and microchannel walls would result in an increase in resistance. In addition, two thermocouples were attached to the test assembly by spot welding: one inside the nozzle, approximately halfway down its

length, and the other attached to the test stand at the base of the ceramic thermal standoffs. The nozzle thermocouple is positioned as close as possible to the hot core of the resistojet – the small size of the nozzle throat prevents direct instrumentation of the interior. The thermocouple at the base measures the temperature rise that would be seen at the spacecraft mounting point due to the thruster operation, taking into account the effect of the mounting configuration with ceramic standoffs for thermal isolation.

3.1 Test setup

Endurance testing was carried out in the David Fearn Electric Propulsion Laboratory at the University of Southampton. The vacuum facility, shown in Figure 4, consists of a main chamber (2 m diameter x 4 m length) and a smaller loading chamber (0.75 m diameter x 0.7 m length) separated by a pneumatically actuated gate to allow for rapid turnaround of hardware from high vacuum to atmosphere and back. The loading chamber was sufficient for endurance testing since no propellant was used. It is equipped with a Leybold TURBOVAC MAG W700 iP turbomolecular pump backed by an Edwards XDS 35i scroll pump with a pumping rate of 40 m^3h^{-1}. Chamber pressure is monitored continuously by a Pfeiffer Vacuum PKR 251 gauge equipped with a Pirani sensor and an inverted magnetron cold cathode gauge, giving a combined range of $5x10^{-9}$ – 1000 mbar.

Figure 4: David Fearn EP Laboratory, vacuum chamber shown in centre.

Electrical power was provided by a Kikusui PWX1500L (PSU), operated in current-controlled mode. The PSU dynamically varies supply voltage to maintain a constant current, up to a specified maximum voltage. The maximum voltage, indicated in Table 3, in effect imposes a maximum power that can be supplied by the PSU. This ensures safety and prevents support equipment damage regardless of the nature of failure mode encountered in the testing. The thrusters were both instrumented identically, with two type K thermocouples, using a National Instruments NI-9213 module in an NI cDAQ-1988XT CompactDAQ chassis for datalogging. The instrumented thruster assemblies are shown in Figure 5. Voltage was measured at the power terminals of the thruster, connected by an electrical feedthrough to a LeCroy Wavesurfer 3024 oscilloscope via a PP020-1 passive voltage probe. The same oscilloscope was used to measure current via a CP030A current prove attached to the power cable near the power feedthrough on the air side. A LabVIEW GUI was developed to control and monitor the resistojet to ensure a consistent and repeatable test sequence. The program uses an input text file to specify a control sequence. All test outputs from the thermocouples, PSU and oscilloscope were collected by the program and output as a single .csv log file. Figure 6 shows a schematic diagram of the endurance test setup.

The measurement uncertainty of the Wavesurfer 3024 oscillocope for this experiment is the sum of DC Gain Accuracy (DCGA) and the Offset Accuracy (OA). These vary depending on the oscilloscope range and therefore must be calculated differently for each experiment due to the different currents and voltages used. In each experiment, the range and offset were configured such that the expected signal was centred on the display, given the available range selections. The corresponding offset and range values are shown in Table 4. The DCGA is given by the Wavesurfer 3000 series datasheet as ± 1.5 % of full scale when the range is > 5 $mVdiv^{-1}$. The OA is given as ±(1.0 % of offset value + 1.5 % full scale + 1 mV). The corresponding values, and the resulting total uncertainty, are shown in Table 4.

Table 4: Oscilloscope electrical measurement configuration and uncertainty

Current (A)	Maximum voltage (mV)	Range (A, mV)	Offset (A, mV)	DCGA (A, mV)	OA (A, mV)	Total uncertainty (A, mV)
15	600	1.6, 160	-15, -600	± 0.024, ± 2.4	± 0.175, ± 9.4	± 0.199, ± 11.8
20	900	4, 400	-20, -900	± 0.06, ± 6	± 0.261, ± 16.0	± 0.321, ± 22.0
25	1200	4, 400	-25, -1200	± 0.06, ± 6	± 0.311, ± 19.0	± 0.371, ± 25.0

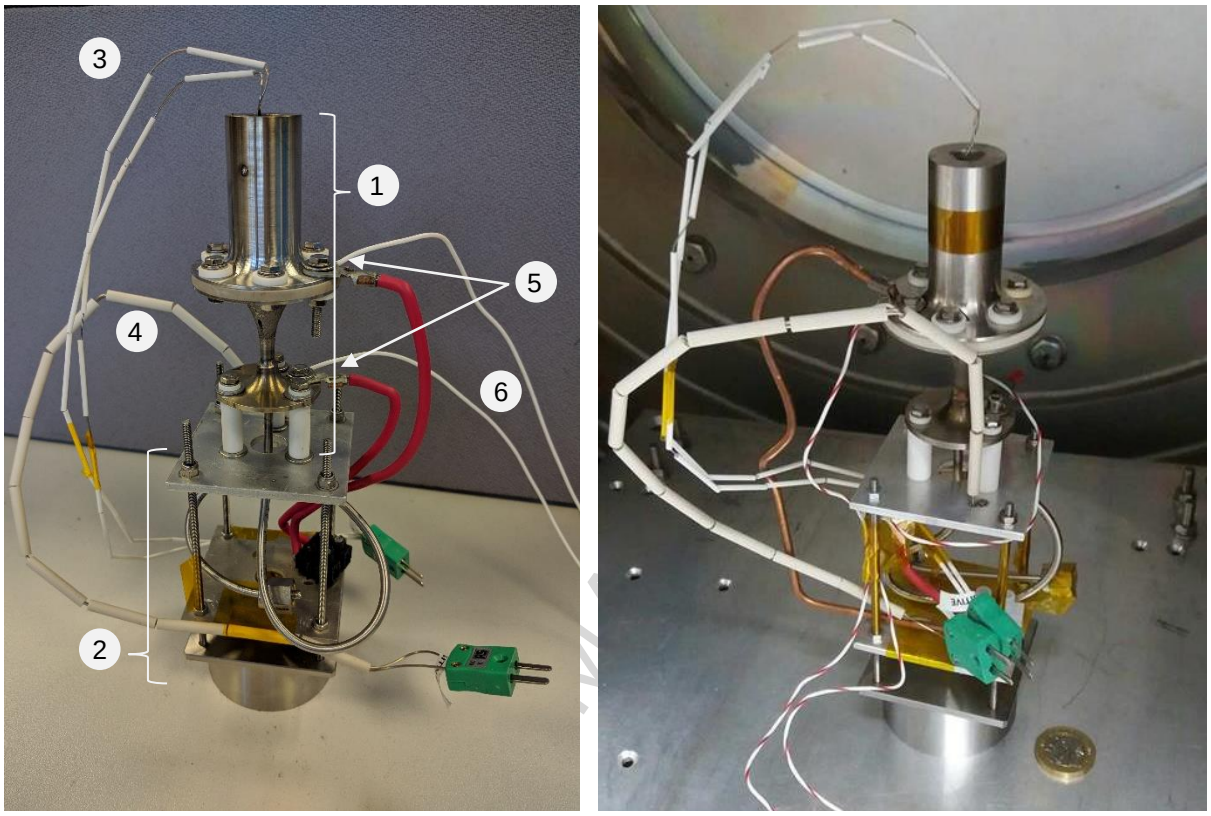

Figure 5: Instrumented thruster test assemblies. STAR-0-B left, STAR-0-C right. Shown on STAR-0-B: 1) thruster assembly; 2) test stand; 3) nozzle thermocouple; 4) interface thermocouple; 5) power terminals; 6) voltage probe leads. Right image includes a British pound coin for scale.

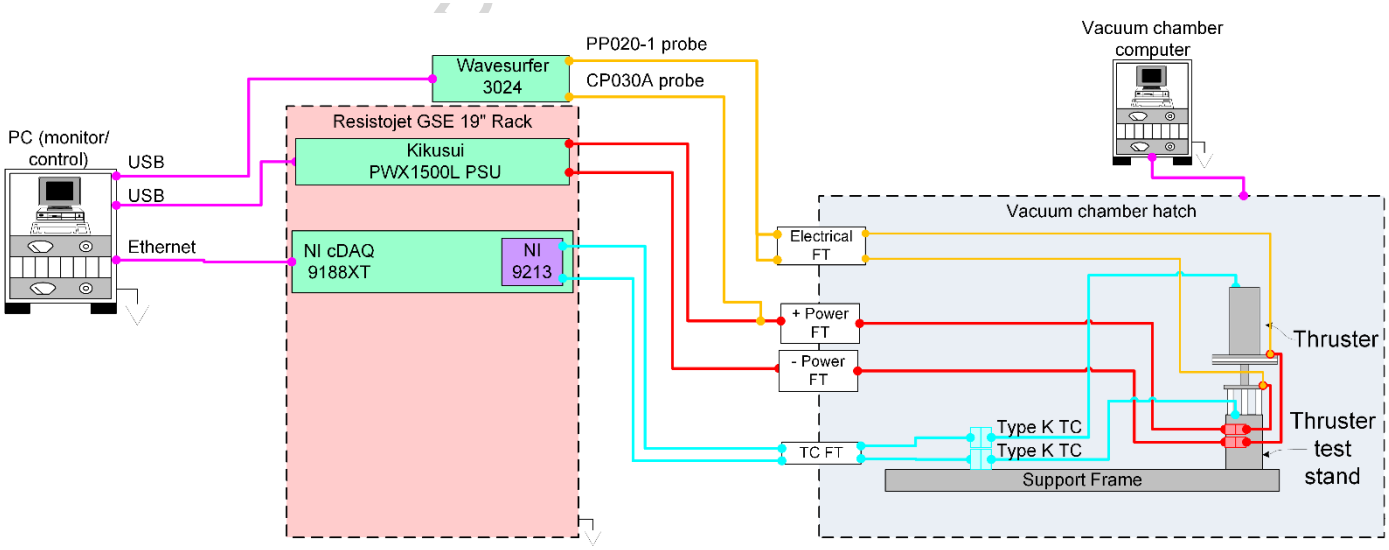

Figure 6: Schematic of endurance test setup. Purple: data connection; orange: oscilloscope measurement; red: power supply; blue: thermocouple measurement.

4. Results and Discussion

In this section, the test results of each thruster will be considered separately. The prototype assemblies will be referred to respectively as STAR-0-B and STAR-0-C, as described in Section 3.

4.1 STAR-0-B Endurance Test Results

STAR-0-B was supplied with 25 A for all cycles. The thruster underwent 78 cycles before the test was stopped due to an observed failure. Figure 7 shows an overview of key test data, with Figures 8 and 9 showing subsets. The upper plot in each figure shows T_n, the temperature at the nozzle thermocouple. The mid plot shows R, resistance between the resistojet terminals calculated from the measured voltage and current. The lower plot shows P_e, electrical power dissipated between the resistojet terminals calculated by multiplying the voltage and current measured by the oscilloscope. Figure 7 shows all 78 cycles of the test, plotted against cumulative heating time (i.e. cumulative time during which the current was applied). The plot omits the cooling periods for clarity, resulting in the discontinuities between each curve, each of which corresponds to one heating period. Three distinct behaviours can be seen in Figure 7, which are distinguished by vertical green lines and classified into stages.

The first stage, labelled "normal operation", begins with the resistojet heating from room temperature and lasts for approximately 40 cycles. In each cycle, T_n increases at an approximate rate of 0.7-0.9 $°Cs^{-1}$, with the heating rate decreasing gradually as temperature increases – however, the nozzle temperature does not reach steady state during the 5-minute heating time. During the first three cycles, the maximum and minimum temperatures during the heating period increase, and thereafter they remain approximately constant between cycles. Resistance rapidly increases in each cycle and, contrary to the nozzle temperature, begins to plateau during the heating phase. As shown in Section 2, over 65 % of the heater's cold resistance results from the two innermost cylinders. This indicates that the inner cylinders heat much more rapidly than the nozzle, approaching their maximum temperature during the heating period, after which their resistance no longer increases. This is supported by observing resistance during the first heating period, which reaches a peak less than 1 mΩ lower than the peaks of subsequent cycles. P_e increases in direct proportion to R during each cycle, since the PSU is operated at constant current. The peak power in each cycle is approximately 30 W. R and P_e reach approximately 90 % of their peak values after 35 s during each cycle.

In the second stage (labelled "onset of degradation"), lasting approximately 15-20 cycles, the resistance R begins to deviate significantly from the profile seen in the first stage. Figure 8 shows the behaviour during this stage in more detail. The overall trend is similar to that in the first stage, with the addition of intermittent and inconsistent decreases in resistance, and corresponding decreases in power. These vary in onset and duration, but are generally of comparable 3-4 mΩ magnitude. This corresponds to a decrease of approximately 10 % in the dissipated power. Since these events are intermittent and the power loss is small, at this stage T_n is not greatly affected, though its peak values in each cycle decreases slightly. Towards the end of this stage, the short circuits become more frequent and severe, and there is a correspondingly greater influence on T_n.

In the third stage, the thruster develops a consistent behaviour different than that of the first stage, as shown in Figure 9. At the beginning of each cycle, R initially increases. After approximately 20 s, there is a rapid drop to circa the initial resistance, after which it continues to increase due to rising temperature. Approximately 60 s later, another, more significant reduction in resistance occurs, to ~5 mΩ below the initial resistance. During the first 5-10 cycles of this stage, this behaviour is inconsistent, thereafter each cycle appears to tend toward a consistent final resistance value .The resistance behaviour shown in stage 3 was used to infer the failure mode. A short-circuit can be caused by contact between two cylinders, creating a bridge through which current can bypass a portion of the heat exchanger. It is proposed that the developing behaviour during the second and third stages is the result of progressively more severe deformation of a cylinder with each thermal cycle, eventually initiating physical contact with another cylinder. In the second stage, this results in an intermittent and inconsistent electrical contact, as asperities on the rough AM surface randomly contact each other. During the onset to the third stage, the deformation of the cylinder becomes great enough to cause firm contact, which, as it develops, decreases the minimum resistance achieved until the cylinders are fully contacting, and the minimum resistance reaches a plateau. Hence, it is proposed that the following mechanism produces resistance patterns consistent with the third stage of behaviour: thermal expansion causes deformation of a cylinder from its axis, resulting in contact with another cylinder shortly into the heating period. This contact is small, and the resistance subsequently continues to rise for a while as the structure heats. This causes additional deformation of the cylinder, perhaps causing pivoting around the initial contact point, until a second more significant contact is made. As the cylinder continues to heat and deform, this increases the contact force, reducing the resistance to its final value. When the heating is discontinued at the end of each cycle, the thruster elastically unloads, however some plastic deformation has occurred leading to the progressive increase in severity.

During testing, the highest temperature seen at the test stand interface thermocouple was 42.34 °C. This peak temperature was reached after 5 cycles, as was the case for T_n, and thereafter the interface temperature varied by less than 1 °C for the remainder of the test, increasing and decreasing due to the heating and cooling periods.

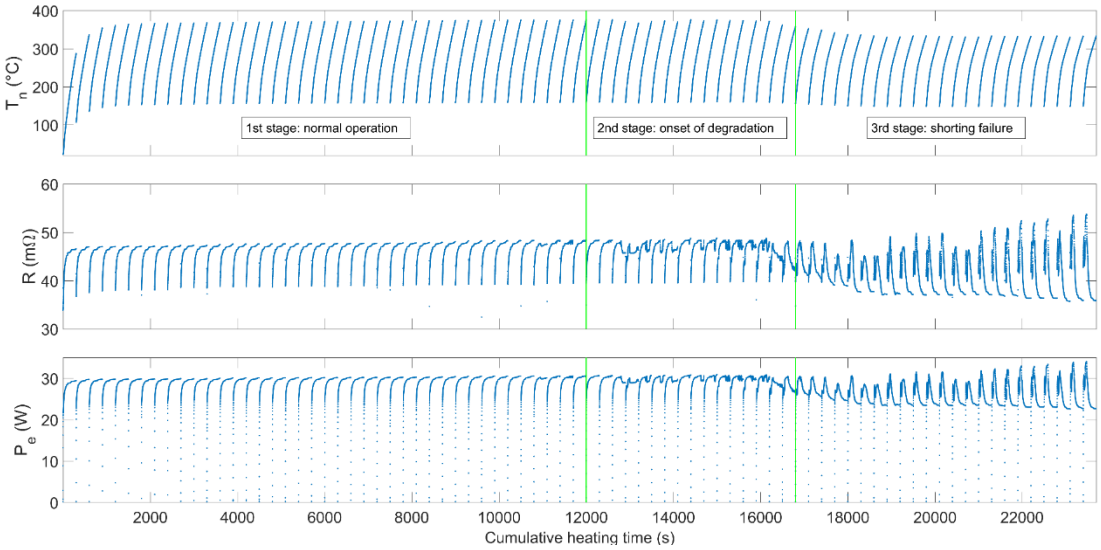

Figure 7: STAR-0-B endurance test overview (cooling periods omitted for clarity). Upper plot: T_n, nozzle temperature; mid plot: R, thruster resistance; lower plot: P_e, thruster electrical power.

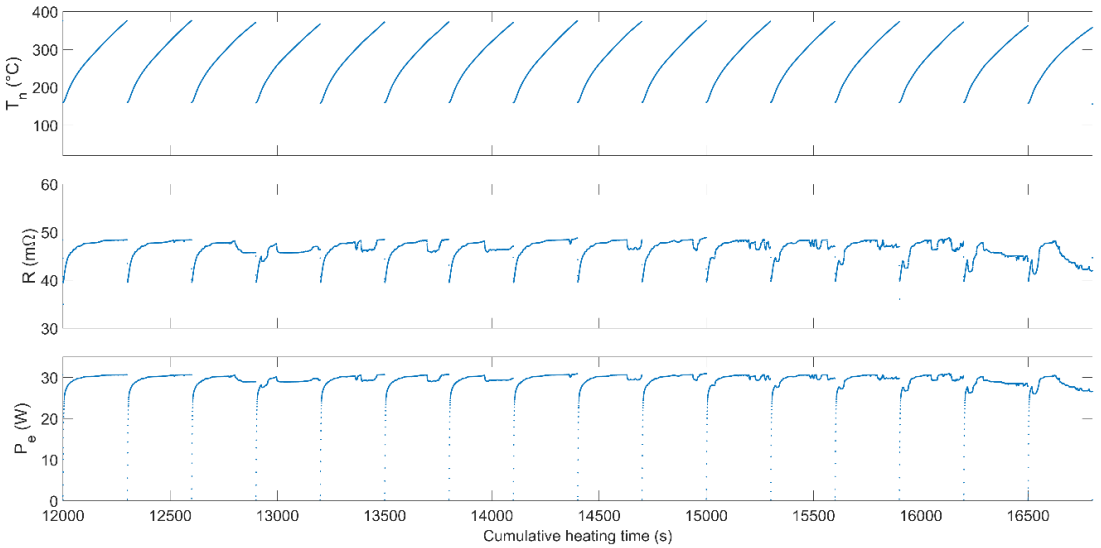

Figure 8: STAR-0-B endurance test second stage: onset of thruster degradation (cooling periods omitted for clarity). Upper plot: T_n, nozzle temperature; mid plot: R, thruster resistance; lower plot: P_e, thruster electrical power.

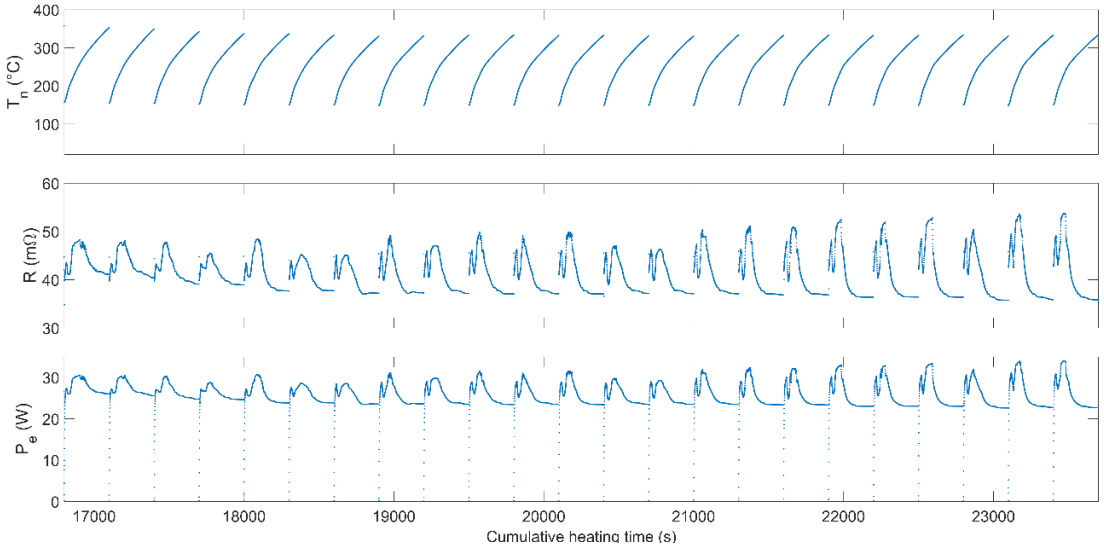

Figure 9: STAR-0-B endurance test third stage: short-circuiting failure mode (cooling periods omitted for clarity). Upper plot: T_n, nozzle temperature; mid plot: R, thruster resistance; lower plot: P_e, thruster electrical power.

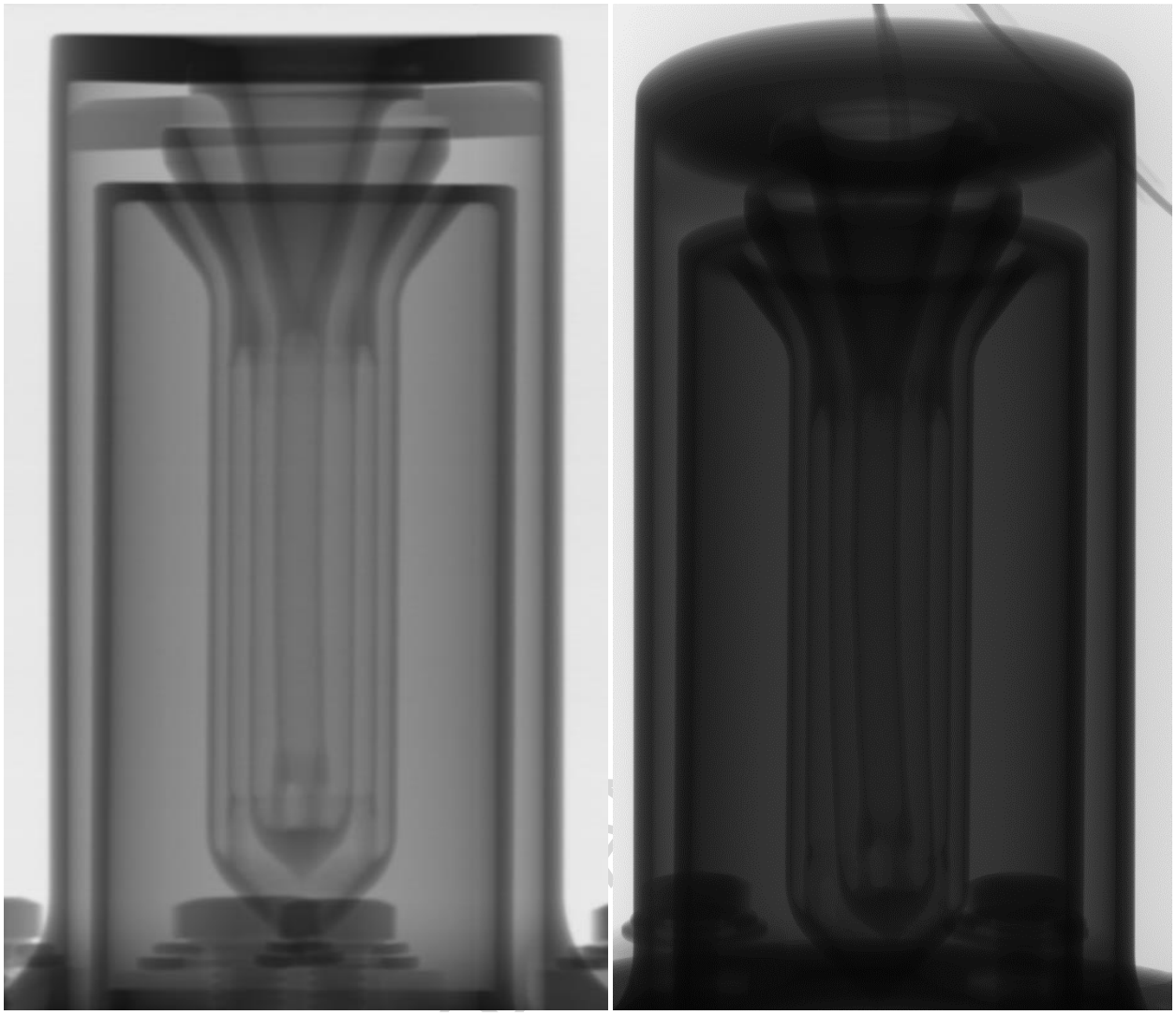

Figure 10: Left: x-ray radiograph of thruster following manufacturing, with slight bow in centre cylinder and straight second cylinder (adapted from [5]). Right: x-ray radiograph of thruster following endurance testing, imaged while cold, showing deformed cylinders.

X-ray CT scans of STAR-0-B following testing revealed that there is off-axis deformation of the inner cylinder. Figure 10 shows a comparison between a micrograph taken at the time of assembly of STAR-0-B and a 3D CT reconstruction of the thruster after failure. Although the latter image is taken with the thruster at room temperature, a permanent bending deformation of the inner two cylinders is clearly visible. It is clear that, if the cylinders bent further, the edge between the second cylinder and its conical tip would eventually contact the inner surface of the third cylinder, resulting in the observed short-circuiting behaviour. A slight initial bow can be seen in the left hand image – this is believed to be caused by the electron beam weld at the nozzle.

Due to the small size of the thruster, it has not yet been possible to directly measure the temperature in the hottest internal parts of the assembly. COMSOL multiphysics models, incorporating electric currents and Joule heating, have been developed to model the heating of the thrust assemblies in both steady state and time-dependent conditions [19]. While rigorous validation remains to be carried out, the models have been used to provide an approximate value for the temperatures at the centre of the thruster. A time-dependent model operating at 25 A indicated a temperature difference of approximately 500 °C between the maximum temperature (in the centre cylinder of the heater) and the position of the thermocouple in the nozzle, after 280 s of heating from room temperature. Applying this estimated difference to the measured T_n of STAR-0-B indicates a maximum temperature of approximately 850 °C in STAR-0-B. At this temperature, 300 series stainless steels exhibit softening and reduced strength which could contribute to the observed deformation.

4.2 STAR-0-C Endurance Test Results

Following the test of STAR-0-B, which failed after only ~1 % of the required cycle life, it was decided to test the second thruster assembly first at lower powers to determine whether the bending and short-circuiting failure mode could be circumvented. Therefore the test sequence shown in Table 3 was implemented, with the plan to test STAR-0-C first at 15 A for 300 cycles, then at 20 A for another 300 cycles, then for the remaining time at full power.

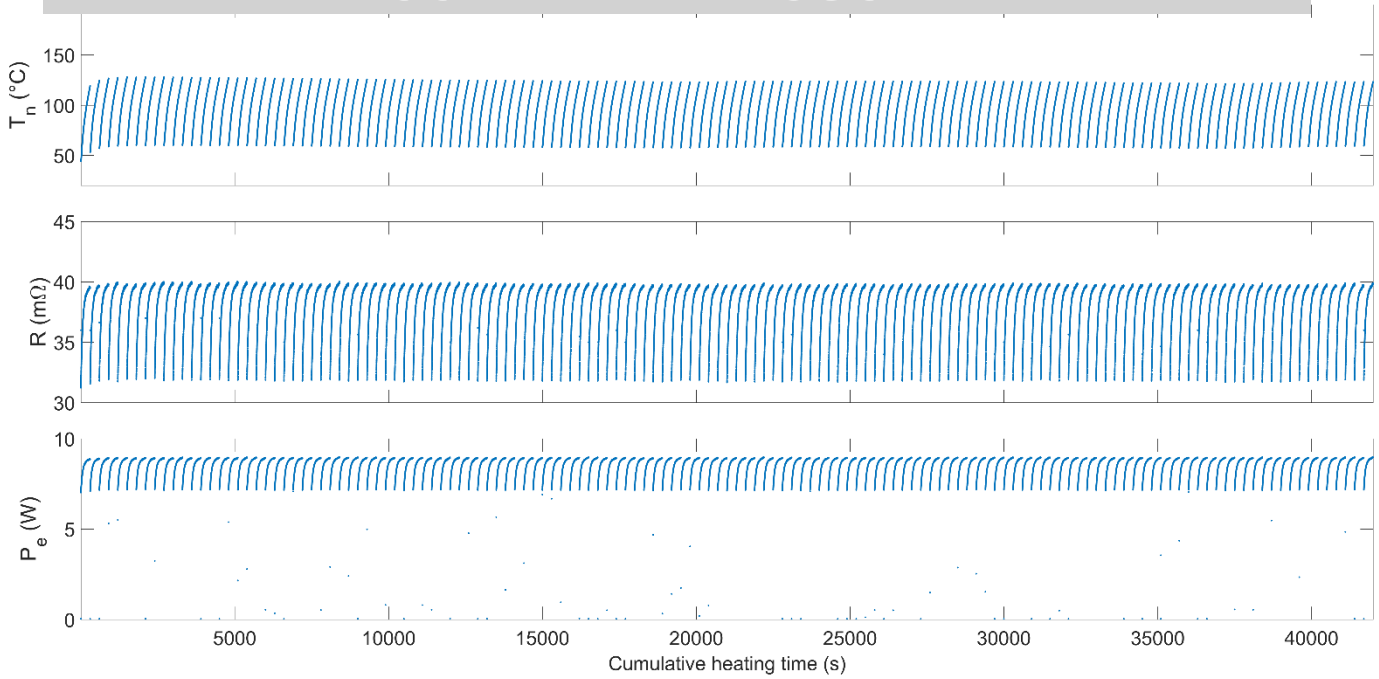

Figure 11: Overview of first 140 cycles of 15 A endurance testing (cooling periods omitted for clarity). Upper plot: T_n, nozzle temperature; mid plot: R, thruster resistance; lower plot: P_e, thruster electrical power.

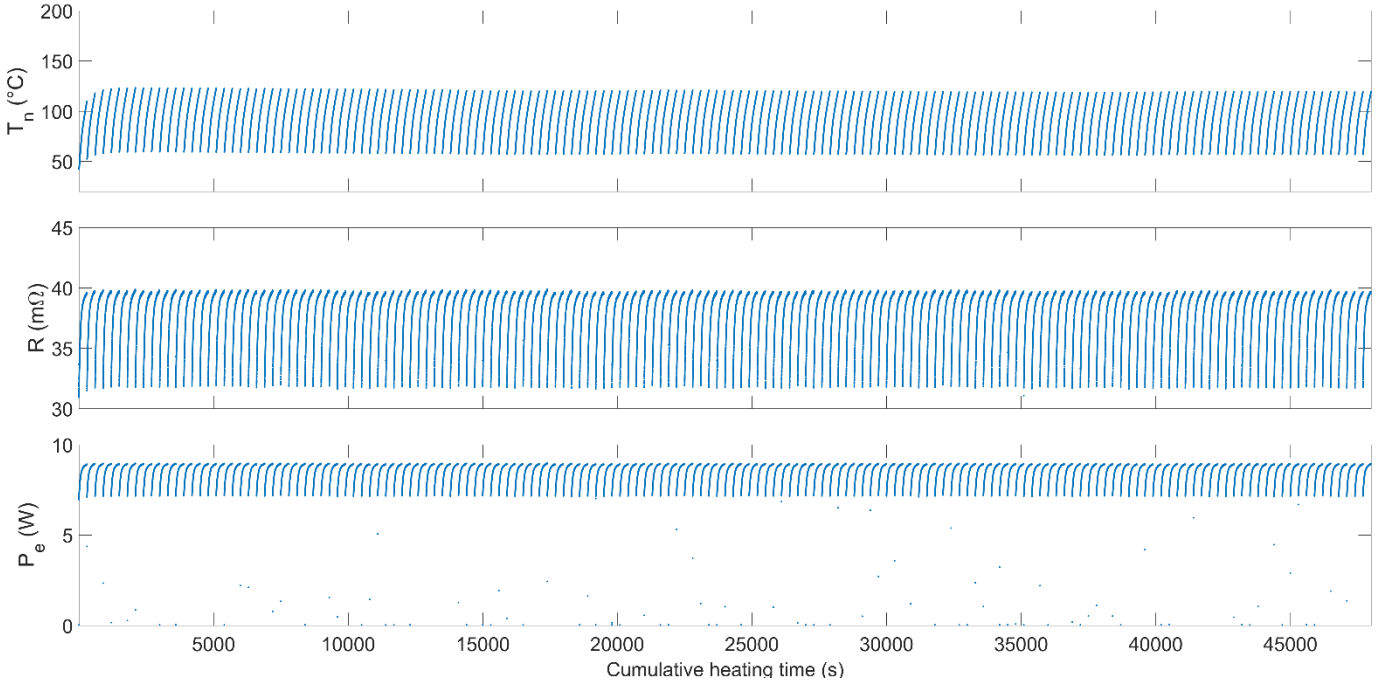

Figure 12: Overview of last 160 cycles of 15 A endurance testing (cooling periods omitted for clarity). Upper plot: T_n, nozzle temperature; mid plot: R, thruster resistance; lower plot: P_e, thruster electrical power.

4.2.1 15 A cycling

Due to practical constraints, the 15 A testing was split into two runs, of 140 and 160 cycles respectively. Figures 11 and 12 show overviews of these runs, with a cumulative 25 hours of heating. The figures are organised in the same way as for STAR-0-B. The behaviour of the thruster matches the first stage of operation of STAR-0-B, at a lower power and temperature. T_n reaches a maximum of approximately 125 °C, while a maximum value of R (approximately 40 mΩ compared to 47 in STAR-0-B) indicates that the core of the thruster also reaches a lower peak temperature than STAR-0-B. Input power is correspondingly lower, reaching a maximum of ~8.9 W. Small fluctuations can be seen in the maximum and minimum temperatures of each cycle – this is attributed to changes in the laboratory temperature during day and night. No failure was observed during the 15 A cycling.

4.2.2 20 A cycling

217 cycles were completed at 20 A, before the test was stopped due to complete failure of the thruster assembly characterised by an open circuit. Figure 13 shows an overview of all 217 cycles, with Figure 14 to Figure 16 showing subsets as described below. Again the behaviour initially matches that seen in STAR-0-B stage 1, and in the STAR-0-C 15 A test runs. T_n reaches a maximum value of approximately 165 °C. The maximum value of R is approximately 42 mΩ, with a corresponding maximum power level of approximately 16.8 W. After approximately 130 cycles, however, the behaviour changes resulting in a failure. Figure 14 shows a cropped view of cycles 133-199, clearly showing an increase in R. The green line in the figure indicates a value of 42 mΩ, approximately the maximum value during the "nominal" cycles at 20 A. By the 195th cycle the maximum resistance has risen to 42.7 mΩ. This increase is small, however the figure shows that it is steady and consistent. This may indicate that the structure of the thruster is deforming in some way that reduces its cross-sectional area at some point, hence increasing the overall resistance. In the latter 5 cycles of Figure 14, the behaviour begins to change entirely. This is shown more clearly in Figure 15.

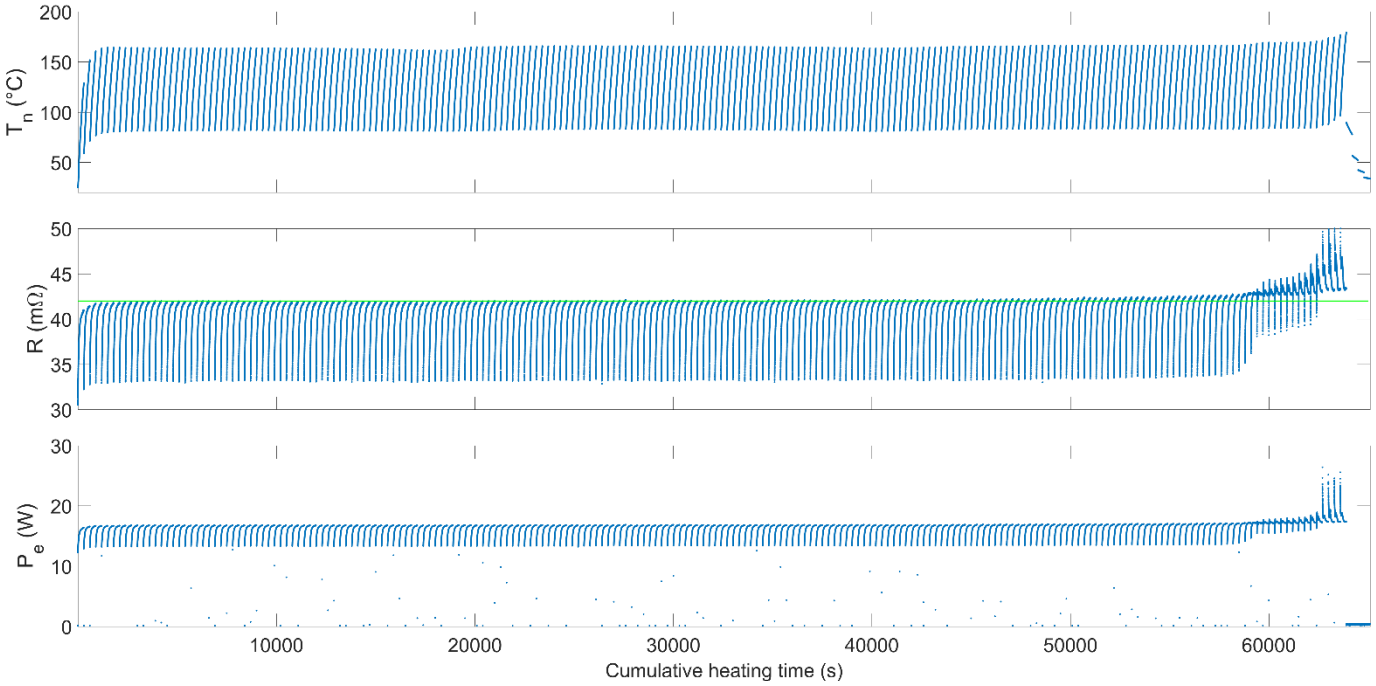

Figure 13: Overview of 20 A testing (217 cycles, cooling periods omitted for clarity). Green line indicates a value of 42 mΩ. Upper plot: T_n, nozzle temperature; mid plot: R, thruster resistance; lower plot: P_e, thruster electrical power.

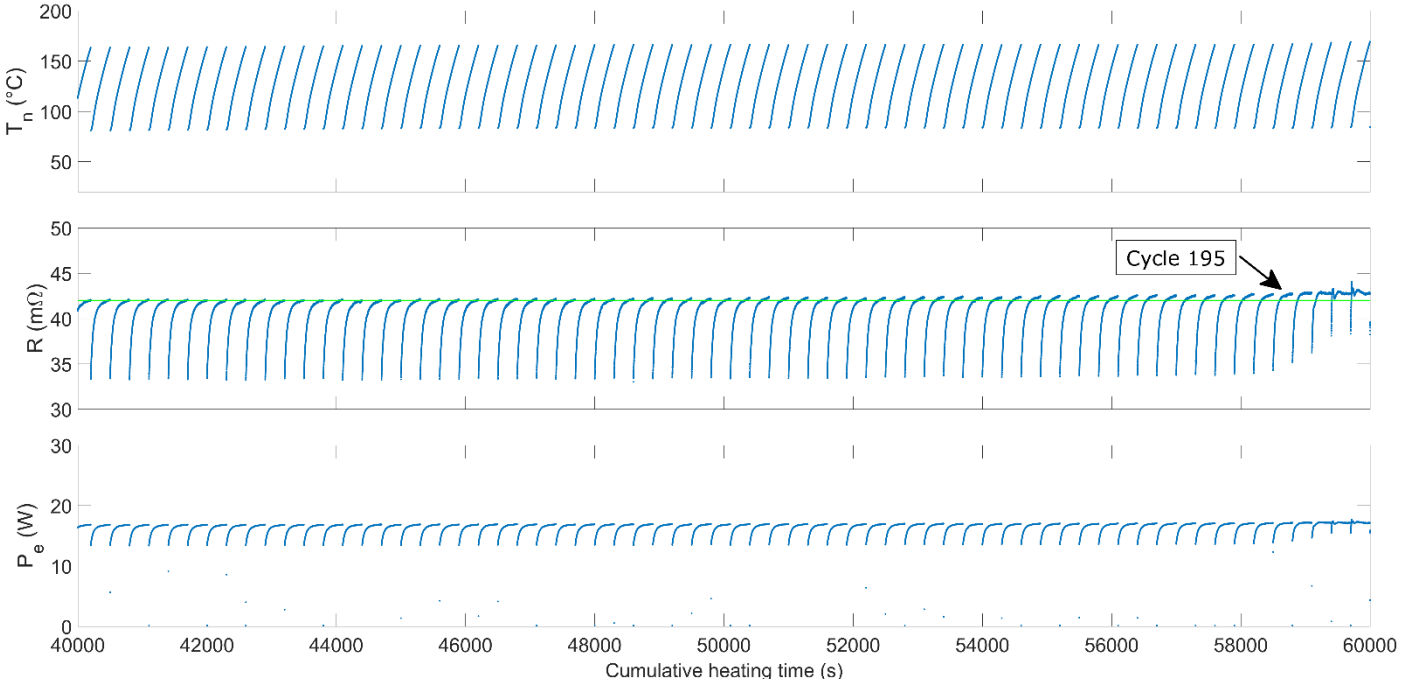

Figure 14: 20 A testing between 40000 and 60000 s cumulative heating time (cycles 133-199). Green line indicates a value of 42 mΩ. Upper plot: T_n, nozzle temperature; mid plot: R, thruster resistance; lower plot: P_e, thruster electrical power.

Figure 15 shows cycles 196 to 213. The remaining 4 cycles are omitted as they are identical to cycle 213. Beginning with cycle 198, the minimum resistance increases significantly. Simultaneously the resistance trend during the cycle also changes, from a smooth increase which plateaus, to an initial sharp increase followed by a decrease. The "hump" that appears becomes progressively more severe, however until cycle 210, each cycle reaches approximately the same steady state value (although this is still gradually increasing as in Figure 14). At cycle 210, this changes, and the initial resistance jumps. The maximum recorded resistance value at the beginning of cycle 210 is 65.57 mΩ. This rapidly decreases, and after approximately 10 s the resistance behaviour returns to the same hump and plateau pattern as before. This behaviour is repeated up to and including cycle 213, with the hump profile changing but the final value remaining approximately constant. Beginning with cycle 214, the resistance is sufficiently high that the power decreases to below 0.5 W.

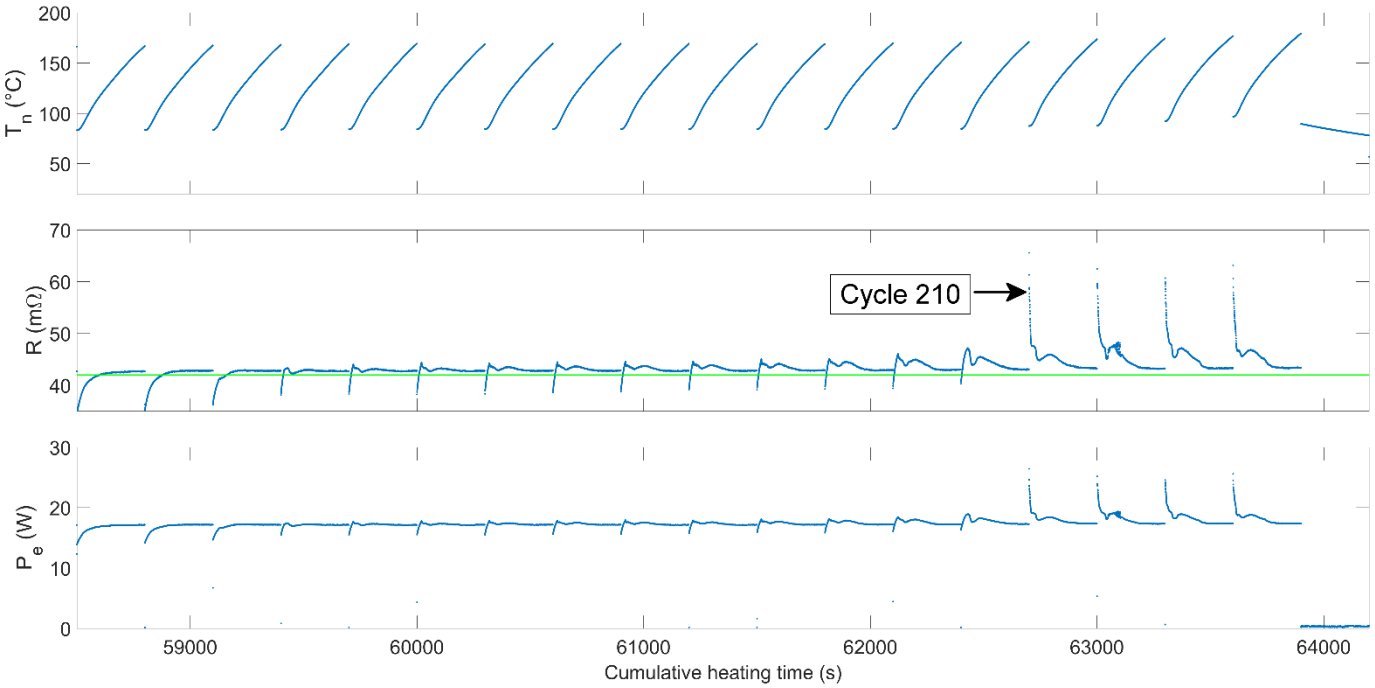

Figure 15: 20 A testing, cycles 196 to 214. Green line indicates a value of 42 mΩ. Upper plot: T_n, nozzle temperature; mid plot: R, thruster resistance; lower plot: P_e, thruster electrical power.

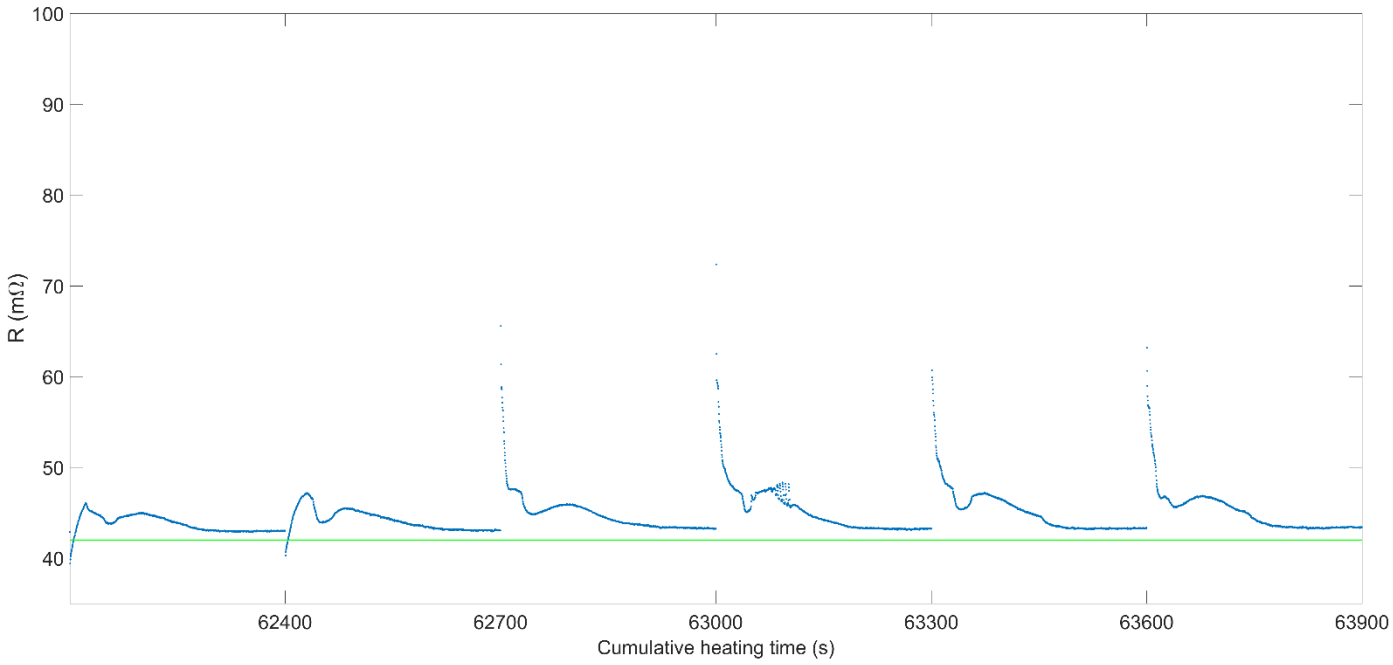

Figure 16: 20 A cycles 208-213, resistance only. Green line indicates a value of 42 mΩ. Upper plot: T_n, nozzle temperature; mid plot: R, thruster resistance; lower plot: P_e, thruster electrical power.

Figure 17: Left: Cutaway of thruster assembly. Red outline shows CT region of interest, and blue line shows location of optical micrograph in Figure 18. Right: Cutaway of 3D CT reconstructions of STAR-0-C before (top) and after (bottom) testing. Connecting struts at centre of image are intact before testing, and fully fractured after.

The resistance trends can again be used to infer a failure mechanism, in this case different to that of STAR-0-B. It is clear that part of the STAR-0-C structure has fractured, leading to an open circuit, and that this failure occurred in stages as shown in Figure 15. This suggested that the fracture occurred in the struts connecting the inner cylinder to the second cylinder, which was confirmed by CT scans as shown in Figure 17. The failure is suspected to be due to out-of-phase thermal fatigue, wherein the maximum temperature of the connecting struts coincides with compressive thermally induced loads, and the minimum temperature corresponds to tensile loads. The proposed failure mechanism is illustrated in Figure 20. As the thruster heats up, the central cylinder (including the struts) is constrained by the surrounding, cooler structure, developing compressive thermal

stresses. These stresses exceed the high-temperature yield strength of the material, leading to plastic deformation. Due to this plastic deformation, when the thruster cools and contracts, tensile stresses are induced. Over a number of cycles, this tensile stress causes initiation and propagation of cracks in the struts. The resistance trends support this proposed damage mechanism - as seen in Figure 14, the initial resistance in each cycle begins to increase, suggesting that the crack is growing with each cycle, reducing the conductive cross-sectional area of the struts. Despite the increase in initial resistance, and the changing trend, in each cycle the final resistance converges to a similar value (42-43 mΩ). This is a result of the crack being closed by compressive stresses upon heating – followed by crack growth upon cooling, leading to the change in behaviour in the subsequent cycle.

Optical micrographs of a polished and etched cross section of the inner channel of the heat exchanger are shown in Figure 18. The section observed in this micrograph is normal to the long axis of the heater, and hence parallel to the AM build plate. A fine cellular dendritic microstructure can clearly be seen in the optical micrograph. This is typical of 316L parts manufactured through SLM, due to the rapid cooling rate of the SLM process (10^5-10^7 Ks^{-1}) which leads to non-equilibrium solidification conditions. Montero-Sistiaga et al investigated the effects of heat treatment on the mechanical properties of 316L produced through SLM [20]. They found that samples treated for 6 hours at 650°C under argon retained their cellular dendritic microstructure, whilst those treated at higher temperatures did not. The samples treated at higher temperatures exhibited lower yield and ultimate strengths comparted to the samples treated at 650°C.

As density of SLM parts reaches nearly full level (>98%), grain size becomes the most important factor to tensile strength [21]. The fine cellular dendritic microstructure of 316L produced through SLM impedes the movement of dislocations throughout the structure, accumulating at boundaries and acting as strengthening sites [20]. The presence of the cellular dendritic microstructure implies that the specimen should have had a high fracture toughness. However, operating at elevated temperatures will have decreased the amount of energy needed for dislocations to become unpinned. Figure 19 shows an SEM image of one of the fracture surfaces of the heater of STAR-0-C. The fracture surface indicates that the specimen most likely failed due to brittle fracture as it lacks the characteristic dimpling surface of a ductile fracture. Within the fracture surfaces can be seen numerous voids ranging in size from 30-50µm. These voids may have been the sites from which failure initiated.

During testing, the maximum temperature recorded by the interface thermocouple was 44.04 °C. As in STAR-0-B the interface temperature reaches its peak value after 5 cycles, and thereafter in each cycle varies by less than 1 °C. In contrast to STAR-0-B, due to the longer duration of the STAR-0-C testing, there was a larger but slower variation in temperature due to the laboratory environment, reducing the interface temperature to approximately 40 °C during the night.

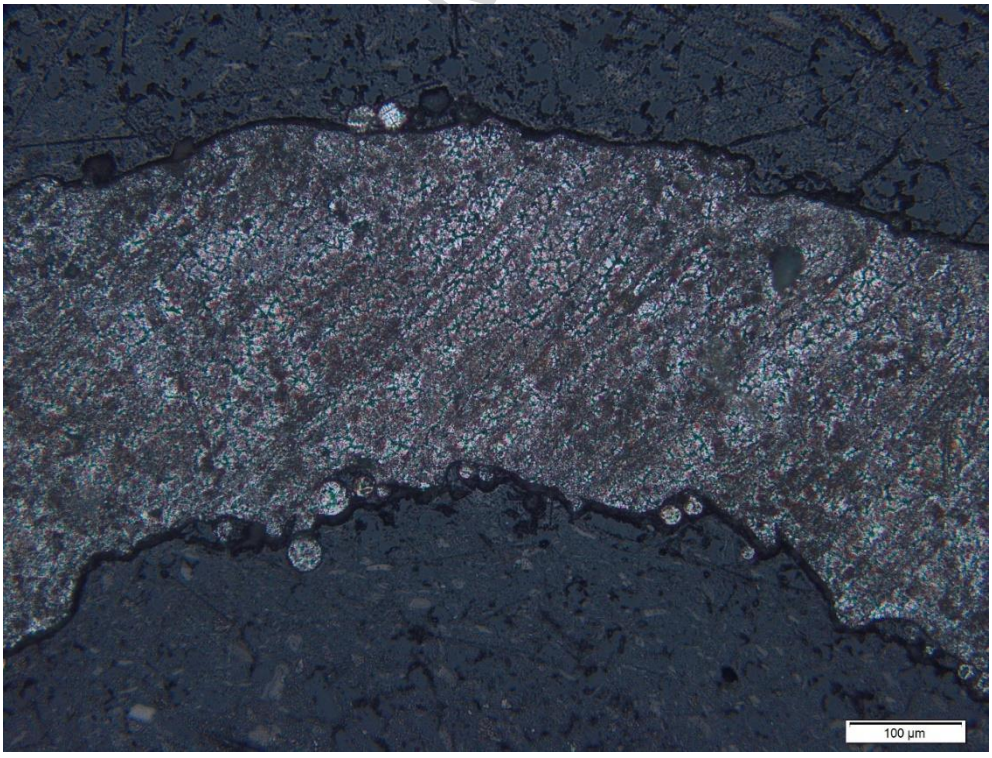

Figure 18: Optical micrograph showing microstructure of central cylinder of STAR-0-C heater post-testing. Position of sample indicated in Figure 17.

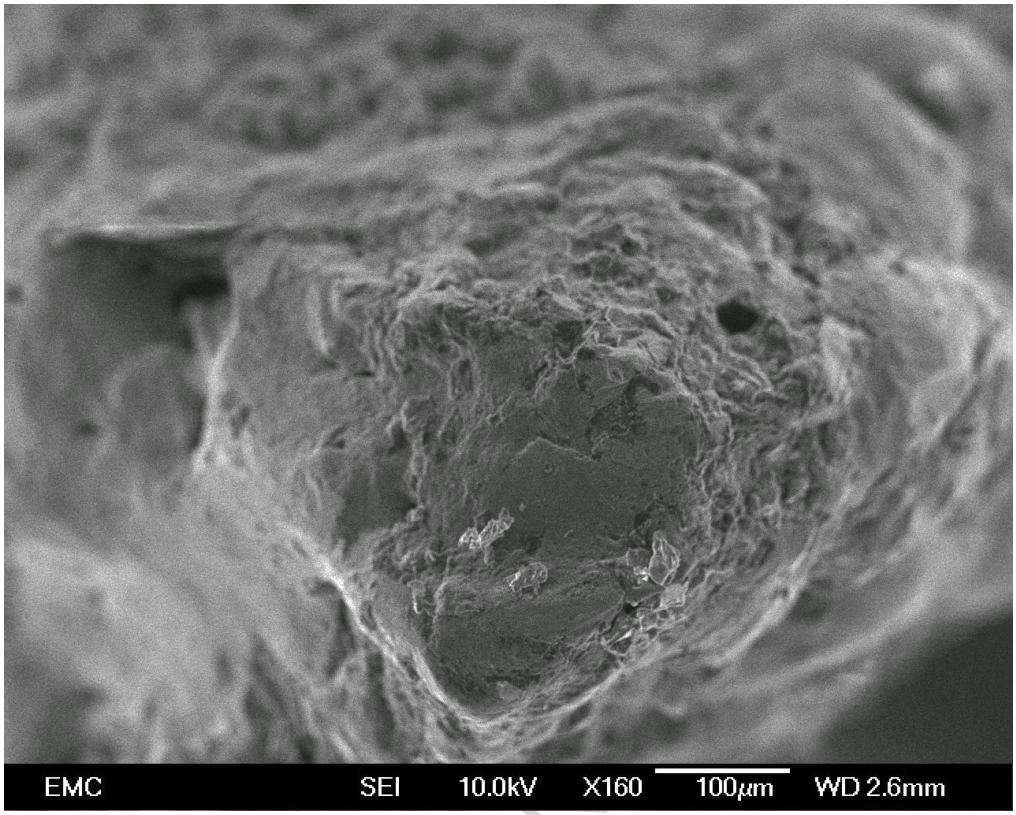

Figure 19: SEM micrograph of fracture surface of STAR-0-C.

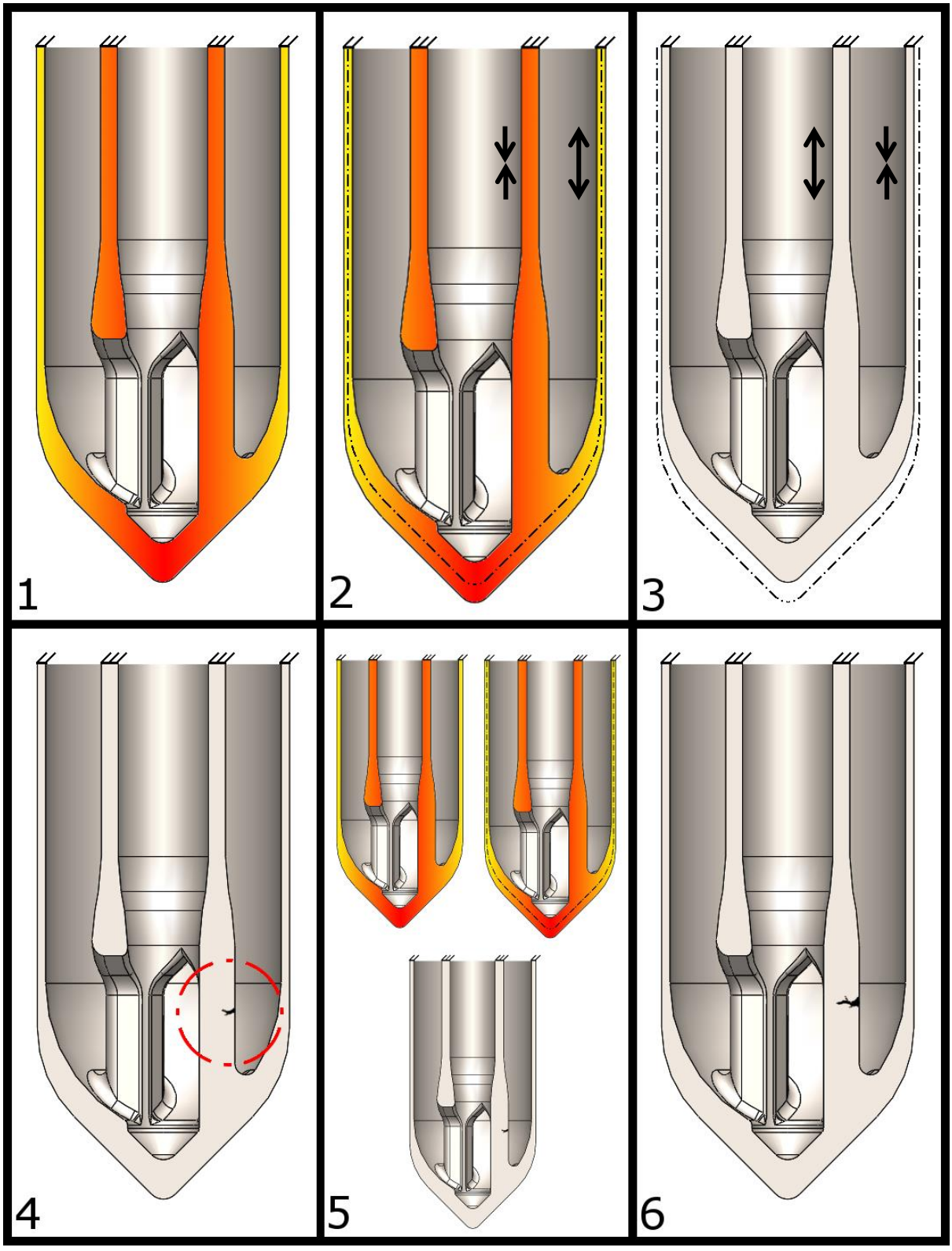

Figure 20: Proposed failure mechanism for STAR-0-C. 1) Electric current heats resistojet. 2) The hotter inner cylinder, constrained in its expansion by the cooler outer cylinders, experiences high compressive stress and yields. 3) When the current is switched off, the resistojet cools and contracts, generating tensile stresses in the inner cylinder. 4) A crack initiates in the connecting strut. 5) The thermal cycle repeats, with the crack closed while hot by compressive thermal stresses. 6) The crack grows.

5. Conclusion

The work has described the results of endurance tests on two prototype resistojets, of a design planned for high-temperature use but currently manufactured in 316L stainless steel for initial prototyping. Both thrusters failed during testing, demonstrating that the current implementation of the thruster design was not able to withstand lifetime requirements for a high-temperature resistojet at the tested currents. STAR-0-B failed after approximately 40 cycles at 25 A, 1 % of the required cycle life for use on the small LEO platform of SSTL. STAR-0-C completed 300 cycles at 15 A, and then failed after approximately 200 cycles at 20 A, confirming that the thruster life can be extended by running at lower power.

Both thrusters exhibited different failure modes, fully described in the discussion. STAR-0-B failed due to the inner cylinders bending when heated, eventually causing a short circuit and reduced power. This failure mode, in operation, would result in reduced performance, but the thruster may remain usable. STAR-0-C failed due to fracture of the three struts connecting the inner and second cylinders in the thruster. The failure is believed to be due to out-of-phase thermal fatigue. Such a failure in operation would completely prevent heating of the thruster, though it may still be possible to use it in cold mode with reduced performance. Electrical resistance measurements and x-ray CT images were used together to diagnose the failure modes of each thruster. Although the prototype thrusters use a material that will not be used in later engineering models, the failure modes observed can be attributed to aspects of the design itself, supported by literature around earlier resistojets of similar design. Therefore, it can be expected that similar failure modes would be seen even in the planned future materials, In718 and refractory alloys.

The results reported here must be taken in context: since only 2 thrusters have been tested, this does not represent an exhaustive analysis of life-limiting failure modes. This is especially the case given the variability that can be expected between AM parts. Moving forward it will be important to perform life tests on several units to gain a more statistically significant picture of the reliability of future STAR designs. Further, it must be noted that the refractory materials required to achieve the high-temperature goals of STAR may give rise to further failure modes not seen in the current stainless steel prototypes. The endurance tests have demonstrated the effectiveness of the combination of resistance and temperature measurements with CT scanning as non-destructive diagnostic tools for the resistojet. The resistance can be used with knowledge of the thruster design to infer structural changes, which can then be directly observed by CT scanning.

The STAR design will be updated in light of this data to attempt to alleviate the root cause of the failure modes described in this paper. This will be achieved by redesigning the heater so that the inner, high-temperature parts are less rigidly constrained, in order to reduce the stresses which develop due to differential thermal expansion. Through a combination of reducing stress and increasing the robustness of the inner parts of the heater (for example by increasing the cross sectional area of the thinnest members), the authors believe an AM concentric cylinder resistojet heater can be developed which will withstand the required lifetime for an operational thruster.

Acknowledgements

The work in this paper forms part of a PhD studentship funded through the Centre for Doctoral Training in Sustainable Infrastructure Systems (CDT-SIS) at University Of Southampton. The funding is provided by the UK Engineering and Physical Sciences Research Council (EPSRC) under grant number EP/L01582X/1, and by H.C. Starck GmbH. Additional funding was provided by the UK Space Agency as part of the RADICAL project, and the National Space Technology Program 2 via Innovate UK. The authors would like to thank Dr Kathryn Rankin, Dr Mark Mavrogordato and Dr Richard Boardman at the University of Southampton's μ-VIS X-Ray Imaging Centre for supporting the use of x-ray CT for non-destructive inspection, and Richard Dooler and Kevin Smith at the University's EDMC workshop for their assistance in manufacturing.

Data availability

The raw data required to reproduce the life testing plots can be found at https://doi.org/10.5258/SOTON/D0798. This data was processed directly into the plots using a MATLAB script.

The raw and processed x-ray CT data cannot be shared at this time due to the large volume of data.

References

[1] A. N. Grubišić, S. Clark, N. Wallace, C. Collingwood, and F. Guarducci, "Qualification of the T6 Ion Thruster for the BepiColombo Mission to the Planet Mercury," in *32nd International Electric Propulsion Conference*, 2011.

[2] M. Coletti, A. Grubišić, C. Collingwood, and S. Gabriel, "Electric propulsion subsystem architecture for an all-electric spacecraft," INTECH, Feb. 2011.

[3] A. N. Grubišić and S. B. Gabriel, "Assessment of the T5 and T6 Hollow Cathodes as Reaction Control Thrusters," *J. Propuls. Power*, vol. 32, no. 4, pp. 810–820, May 2016.

[4] W. A. Hoskins *et al.*, "30 years of electric propulsion flight experience at Aerojet Rocketdyne," in *Proceedings of 33rd International Electric Propulsion Conference*, 2013, pp. 1–12.

[5] D. Nicolini, "Xenon Resistojets as Secondary Propulsion on EP Spacecrafts and Performance Results of Resistojets Using Xenon," in *Proceedings of 28th International Electric Propulsion Conference*, 2003.

[6] F. Romei, A. N. Grubišić, and D. Gibbon, "Manufacturing of a high-temperature resistojet heat exchanger by selective laser melting," *Acta Astronaut.*, vol. 138, pp. 356–368, 2017.
[7] F. Romei, A. N. Grubišić, and D. Gibbon, "High performance resistojet thruster: STAR Status Update," in *Proceedings of Space Propulsion 2018*, 2018.
[8] F. Romei, A. Grubišić, D. Gibbon, O. Lane, R. A. Hertford, and G. Roberts, "A Thermo-fluidic Model for a Low Power Xenon Resistojet," Jul. 2015.
[9] F. Romei, A. Grubišić, D. Lasagna, and D. Gibbon, "Multiphysics model validation of resistojets with concentric tubular heat exchanger," in *7th European Conference for Aeronautics and Space Sciences (EUCASS 2017)*, 2017.
[10] F. Romei, A. Grubišić, and D. Gibbon, "Performance testing and evaluation of a high temperature xenon resistojet prototype manufactured by selective laser melting," in *Proceedings of 35th International Electric Propulsion Conference*, 2017.
[11] C. Ogunlesi *et al.*, "Novel Non-Destructive Inspection of the STAR Additively Manufactured Resistojet," in *Proceedings of Space Propulsion 2018*, 2018.
[12] G. R. Pfeifer, "Technology Development and Demonstration of a Low Thrust Resistojet Thruster," 1972.
[13] D. G. Philips, "Technology Development of a Biowaste Resistojet Volume II," Van Nuys, CA, 1972.
[14] R. J. Page, C. R. Halbach, and M. L. Ownby, "Life test of six high temperature resistojets," in *AIAA 7th Electric Propulsion Conference*, 1969.
[15] R. Y. Yoshida, C. R. Halbach, and C. S. Hill, "Life test summary and high-vacuum tests of 10-mlb resistojets," *J. Spacecr. Rockets*, vol. 8, no. 4, pp. 414–416, 1971.
[16] W. E. Morren, M. V Whalen, and J. S. Sovey, "Performance and endurance tests of a laboratory model multipropellant resistojet," *AIAA J. Propuls. Power*, vol. 6, no. 1, pp. 18–27, 1990.
[17] R. J. Slutz, "A 10,000-hr Life Test of an Engineering Model Resistojet," 1990.
[18] R. K. Desu, H. Nitin Krishnamurthy, A. Balu, A. K. Gupta, and S. K. Singh, "Mechanical properties of Austenitic Stainless Steel 304L and 316L at elevated temperatures," *J. Mater. Res. Technol.*, vol. 5, no. 1, pp. 13–20, Jan. 2016.
[19] F. Romei and A. Grubisic, "Numerical study of a novel monolithic heat exchanger for electrothermal space propulsion," *Acta Astronaut.*, vol. 159, pp. 8–16, Jun. 2019.
[20] M. Montero-Sistiaga, S. Nardone, C. Hautfenne, and J. Van Humbeeck, "Effect of heat treatment of 316L stainless steel produced by Selective Laser Melting (SLM)," in *Solid Freeform Fabrication Symposium*, 2016.
[21] Y. Zhong, L. Liu, S. Wikman, D. Cui, and Z. Shen, "Intragranular cellular segregation network structure strengthening 316L stainless steel prepared by selective laser melting," *J. Nucl. Mater.*, vol. 470, Dec. 2015.

Graphical abstract

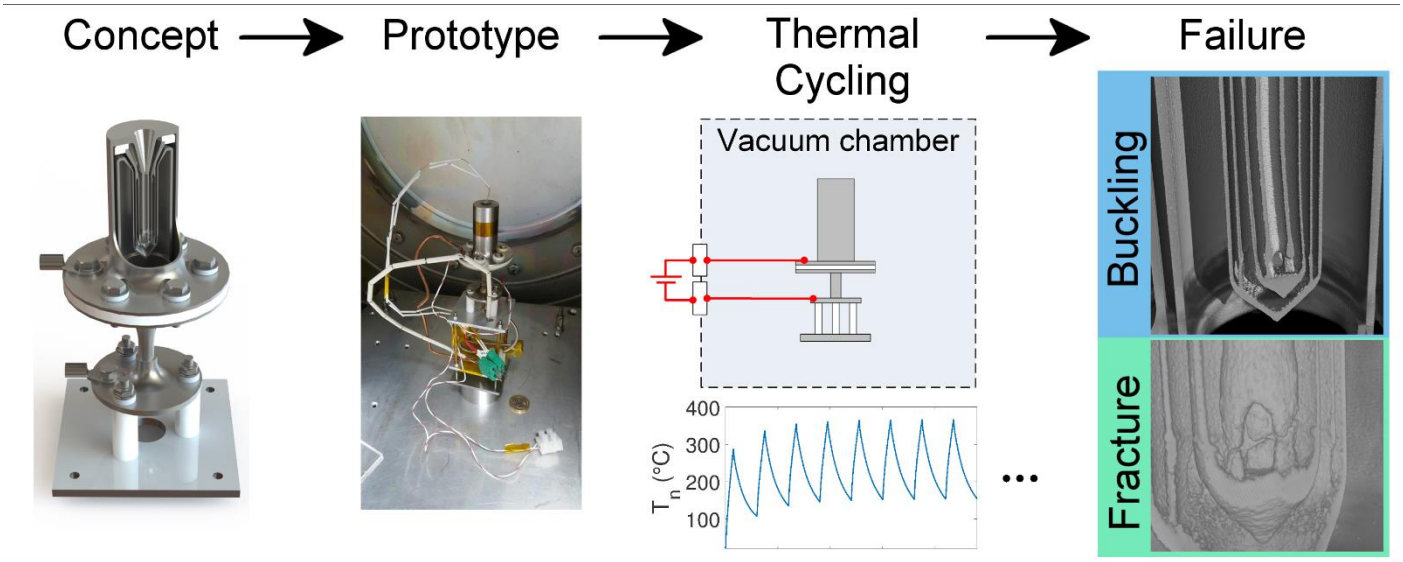

Highlights

- A novel additive-manufactured resistojet thruster design is tested to investigate cycle life under high-temperature conditions.
- X-ray computed tomography and in-situ electrical measurements are combined to diagnose failure modes of the additive-manufactured heater.
- Thermomechanical stresses are found to cause premature failure in additive-manufactured heaters from 316L stainless steel.